



JOURNAL OF
APPLIED
CRYSTALLOGRAPHY

Volume 53 (2020)

Supporting information for article:

Bragg coherent imaging of nanoprecipitates: role of superstructure reflections

Maxime Dupraz, Steven J. Leake and Marie-Ingrid Richard

S1. Case of semi coherent and incoherent precipitates

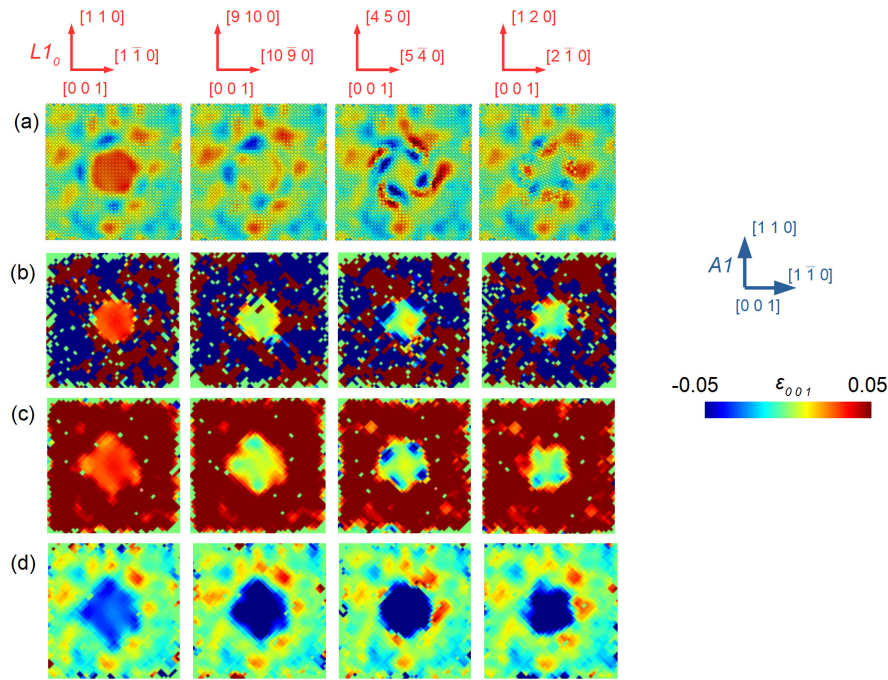


Figure S1 Comparison of the ε_{001} strain component after relaxation for several FCT coherent and semi-coherent nanoprecipitates. The misorientation between the AI matrix and the LI_0 nanoprecipitate increases from left to right inducing a gradual loss of coherency. (a) ε_{001} atomic strain component calculated from the relaxed atomic positions (b) ε_{001} calculated from equations. (1-2) for $\mathbf{g} = 0\ 0\ 1$ using the FCT lattice as a reference for the calculation. (c-d) ε_{001} calculated from equations. (1-2) for $\mathbf{g} = 0\ 0\ 2$ using the FCT and FCC as references for the calculation respectively

Figure S1 and **Table S1** show the influence of the coherency between the AI matrix and the LI_0 nanoprecipitate on the ε_{001} strain component. A nanoprecipitate of radius $r = 2.22$ nm is inserted at the centre of a $11 \times 11 \times 11$ nm³ simulation cell, and the strain distribution is shown in the $(0\ 0\ 1)$ crystallographic plane after energy minimization. The structure and composition of the AI matrix is identical in the four configurations, while the FCT LI_0 nanoprecipitates are inserted with an increasing degree of in-plane misorientation, corresponding to a rotation around the c -axis (Z_m $[0\ 0\ 1]$ and Z_p $[0\ 0\ 1]$ crystallographic directions of the AI and LI_0 matrix respectively). In the initial configuration, the misorientation angle θ between the AI and LI_0 phases varies in the range of 0° ($X_m = X_p = [1\ \bar{1}\ 0]$), corresponding to a fully coherent nanoprecipitate, to 18.43° ($X_m[1\ \bar{1}\ 0], X_p[2\ \bar{1}\ 0]$, **Table S1**). Note that for a small misorientation ($X_p[10\ \bar{9}\ 0]$, $\theta = 3.01^\circ$), the nanoprecipitate tends to rotate - during the relaxation in order to minimize the interfacial energy between the matrix and the nanoprecipitate.

Table S1 Evolution of $\overline{\varepsilon}_{001}$ in a FCT LI_0 nanoprecipitate ($r = 2.22$ nm) as a function of the misorientation angle between the AI and LI_0 phases.

X_p	θ (°)	$\overline{\varepsilon}_{001}$ / ref FCT (%)	$\overline{\varepsilon}_{001}$ / ref FCC (%)
$[1\ 0\ \bar{1}]$	0	3.71	-2.96
$[1\ \bar{1}\ 0]$	0	3.79	-2.88
$[20\ \bar{1}9\ 0]$	1.47	3.13	-3.51
$[10\ \bar{9}\ 0]$	3.04	2.48	-4.12
$[4\ \bar{5}\ 0]$	6.34	0.46	-6.00
$[1\ \bar{2}\ 0]$	18.43	1.20	-5.31

As illustrated in **Figure S1a** & **Table S1**, which show the ε_{001} atomic strain distribution calculated from the relaxed atomic positions, the strain distribution for the coherent nanoprecipitate LI_0 $[1\ \bar{1}\ 0]$ \parallel AI $[1\ \bar{1}\ 0]$ is almost identical to the one obtained for the $[1\ 0\ \bar{1}]$ variant. A tensile strain builds up in the nanoprecipitate during relaxation (from $\overline{\varepsilon}_{001} = +3.71\%$ to $\overline{\varepsilon}_{001} = +3.79\%$), associated to an increase of the $\frac{c}{a}$ ratio from 0.92 to 0.953. This value is slightly lower than the one reported in section I of Results ($\overline{\varepsilon}_{001} = +4.1\%$) which was obtained for a smaller nanoprecipitate ($r = 1.755$ nm). Note that this decrease of the tensile strain during the nanoprecipitate coarsening is consistent with the experimental observations of (Garcia-Gonzalez *et al.* 2019). The loss of coherency between the AI and LI_0 phases has a dramatic effect on the strain distribution in the nanoprecipitate (**Figure S1** & **Table S1**). A misorientation as small as 1.47° results in a drop in the tensile strain of 0.6% (from 3.79% to 3.13%). Further increasing the misorientation induces a further drop of the tensile strain which drops to 0.46% for $\theta = 6.34^\circ$. This relaxation of the misfit elastic strain is associated to the formation of interfacial dislocations which results in a heterogeneous strain distribution in the nanoprecipitate. The matrix on the other hand does not evolve during relaxation ($\overline{\varepsilon}_{001} \approx 0\%$) and is also mostly independent of the misorientation between the AI and LI_0 phases (**Figure S1a,d**). However, the formation of misfit dislocations induced by the loss of coherency also results in a more heterogeneous strain distribution in the matrix. The latter is well visible for $\theta = 6.34^\circ$ where a tensile strain builds up in several regions in the vicinity of the precipitate.

Finally, the calculation of the strain maps from equation (2) reveals an excellent agreement with the atomic strain distribution shown in **Figure S1a**. Using the FCT lattice as a reference for the strain calculation, one obtains a strain distribution very consistent with the calculation from the relaxed atomic positions in the ordered LI_0 phase for both superstructure ($g = 0\ 0\ 1$, **Figure S1b**) and fundamental ($g = 0\ 0\ 2$, **Figure S1c**) reflections. For the latter, a large tensile strain is observed in the

Al matrix corresponding to the initial lattice mismatch between the *Al* and *L1₀* phases ($\overline{\varepsilon_{001}} \approx 6.9\%$). On the other hand, using the FCC lattice reveals an excellent agreement with the calculation from the relaxed atomic positions in the disordered *Al* phase (**Figure S1d**).

S2. Influence of the choice of the RSV on the retrieved Bragg electron density

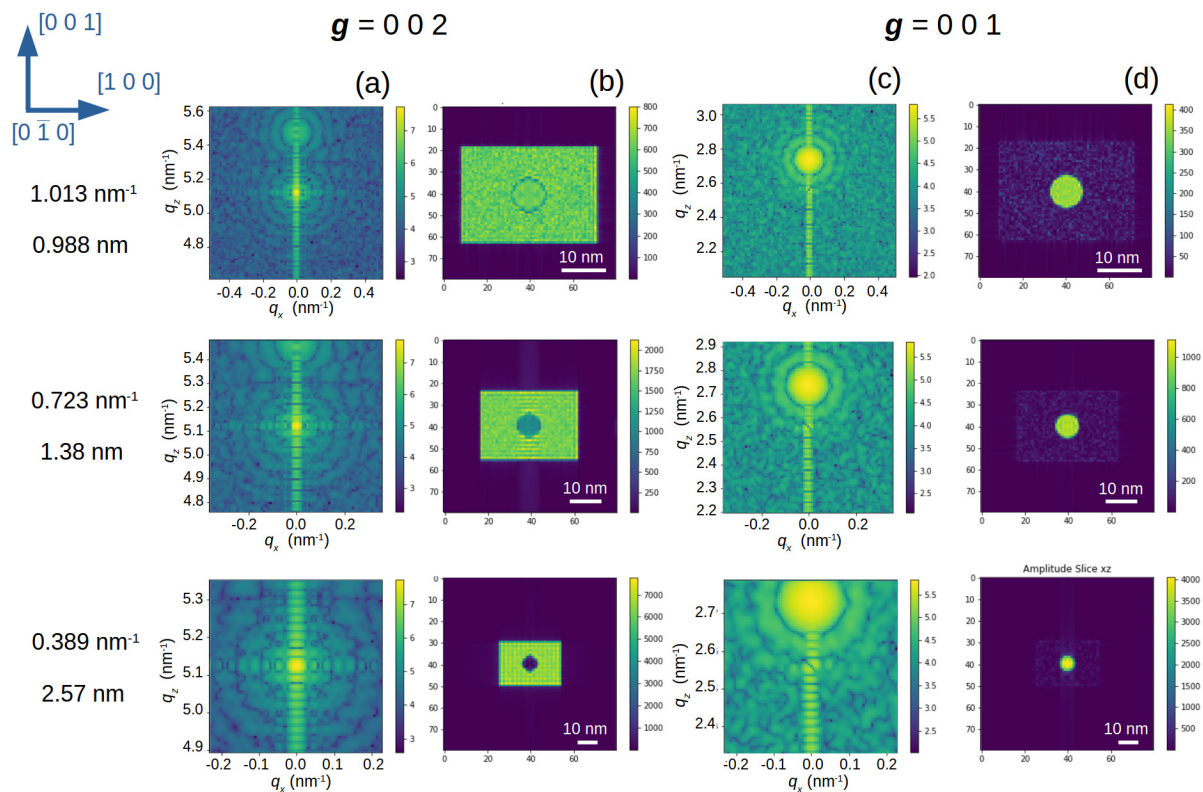


Figure S2 Influence of the extent of the RSV on the retrieved Bragg electron density. From top to bottom the RSV is gradually decreased which translates in the real space in an increase of the voxel size. (a) Calculated diffraction pattern from equation (1) for $\mathbf{g} = 0\ 0\ 2$. (b) Retrieved Bragg electron density from equation (2) ($\mathbf{g} = 0\ 0\ 2$). (c) Calculated diffraction pattern from equation (1) for $\mathbf{g} = 0\ 0\ 1$. (d) Retrieved Bragg electron density from equation (2) ($\mathbf{g} = 0\ 0\ 1$). The perfect FCC lattice is used as a reference in all cases. The numbers at the left side indicate the extent of the RSV in reciprocal space and the voxel size in real space.

Given the small size of the nanoprecipitates considered in this work, a very high spatial resolution ($< 1\text{ nm}$) is necessary in order to image accurately the strain distribution in the nanoprecipitates. Achieving such high spatial resolution requires the computation of large RSVs. As a consequence, for a voxel size below 1 nm (corresponding to a RSV larger than $1 \times 1 \times 1\text{ nm}^{-3}$), the intensities scattered by the disordered matrix and the ordered nanoprecipitate are both included in the computed RSVs, independently of the choice of the reference lattice for the calculation. Hence, despite the large lattice mismatch between the Al and Li_0 phases ($\sim 6.9\%$), performing the calculation in the vicinity a fundamental reflection (e. g., $\mathbf{g} = 0\ 0\ 2$, **Figure S2a**) allows to retrieve the Bragg electron density of both phases accurately (**Figure S2b**). If the same FCC reference lattice is used, but the calculation is performed on a smaller RSV ($0.723 \times 0.723 \times 0.723\text{ nm}^{-3}$), a fraction of the intensity scattered by nanoprecipitate is outside the computed RSV (**Figure S2a**). Therefore, the integrated, Bragg electron

density of the LI_0 phase decreases by approximately 20% for $g = 0\ 0\ 2$ (**Figure S2b & Table S2**). Such decrease is consistent with the decrease of the integrated scattered amplitude in the reciprocal space (**Table S2**). In contrast, the Bragg electron density of the disordered AI phase is not affected since the RSVs is centred around the centre of mass of the AI FCC peak. On the other hand, the intensity scattered by the nanoprecipitate in the vicinity of a lower order superstructure reflection ($g = 0\ 0\ 1$), is still fully included in the RSV (**Figure S2c**). The integrated Bragg electron density is hence equal to the one obtained for the large RSV (**Figure S2d & Table S2**). With a further decrease of the RSV ($0.389 \times 0.389 \times 0.389\text{ nm}^{-3}$), corresponding to a voxel size equivalent to the experimental one, the intensity scattered by the nanoprecipitate around $g = 0\ 0\ 2$ (**Figure S2a**) is almost completely outside the computed RSV.

Table S2 Influence of the RSV on the integrated scattered amplitudes and integrated Bragg electron densities. For each RSV, the integrated amplitudes and Bragg electron densities are calculated using the FCC and FCT reference lattice. The ratio of the values obtained for the two reference lattices are reported in the Table.

RSV (nm^{-3})	Voxel size (nm^{-1})	($A_{001_FCC} / A_{001_FCT}$) (%)	($A_{002_FCC} / A_{002_FCT}$) (%)	($\rho_{int_001_FCC} / \rho_{int_001_FCT}$)(%) (threshold 25%)	($\rho_{int_002_FCC} / \rho_{int_002_FCT}$)(%) (threshold 25%)
0.39x0.39x0.39	2.57	86.3	10.8	94.1	5.1
0.46x0.46x0.46	2.17	98.6	14.7	98.7	10.8
0.56x0.56x0.56	1.78	100.7	23.0	99.1	21.3
0.72x0.72x0.72	1.38	101.5	80.3	99.1	79.6
1.01x1.01x1.01	0.99	101.8	102.2	99.7	100.1

Therefore, the Bragg electron density drops to an exceedingly small value in the ordered region (5% of its original value), while it is still not affected in the disordered matrix (**Figure S2b & Table S2**). For the superstructure reflection, $g = 0\ 0\ 1$, a fraction of the intensity scattered by the nanoprecipitates is outside the RSV (**Figure S2c**) resulting in a small drop of the integrated Bragg electron density (**Figure S2d & Table S2**).

In a state of the art BCDI experiment, the RSV that is measured around a reflection of interest typically ranges between $0.05 \times 0.05 \times 0.05\text{ nm}^{-3}$ (20 nm voxel size) and $0.3 \times 0.3 \times 0.3\text{ nm}^{-3}$ (3 nm voxel size). Note that the voxel size does not represent the actual resolution of the reconstructed data, the latter being controlled by the dynamic range of the data and the signal to noise ratio (Carnis *et al.* 2019). In the AuCu system, reconstructing simultaneously and accurately the ordered and disordered phases require to measure a RSV larger than $1 \times 1 \times 1\text{ nm}^{-3}$ in the vicinity of a fundamental reflection. Given the fact that most of the time the scattering intensity decreases rapidly with q ($\sim q^{-4}$) away from the Bragg peak and given the available coherent flux on 3rd generation synchrotron beamlines, maintaining a high enough dynamic range and signal to noise ratio over such a large range of the reciprocal space would require extremely long exposure times. In addition, a large lattice mismatch also implies that the coherency between the AI and LI_0 phases is rapidly lost during the coarsening of

the nanoprecipitates (for a nanoprecipitate radius as small as few nanometres). Hence, the imaging of coherent nanoprecipitates in systems with a large lattice mismatch inherently requires measuring larger RSVs than the volumes typically measured in a state of the art BCDI experiment. With the current capabilities of the technique, the accurate and simultaneous measurements of both ordered and disordered phases in systems such as AuCu would be extremely challenging.

On the other hand, in many systems containing coherent precipitates, the lattice mismatch between the ordered and disordered phases is much smaller, making them better candidates for BCDI. In Ni-based superalloys or ferritic steels for instance, the lattice mismatch is well below 1%, which allows to retain the coherency between the ordered and disordered phases during the coarsening of the nanoprecipitates up to sizes of more than 500 nm. In such systems, performing BCDI on a fundamental reflection allows to measure simultaneously the ordered and disordered phases, even if the measurement is performed on a small RSV. Moreover, the gain in brilliance offered by 4th generation synchrotron sources foresees the possibility to probe larger RSVs, with a signal to noise ratio that is still suitable for the technique (Carnis *et al.* 2019). The measurement of such large RSVs is critical to achieve a spatial resolution appropriate for systems where the coherent nanoprecipitates size does not exceed few tens of nanometres. In addition, measuring large RSVs should facilitate the acquisition of the experimental data, by allowing the simultaneous measurement of the ordered and disordered phase in the vicinity of a fundamental reflection.

S3. Illustration of the choice of the reference lattice on the calculated reciprocal space intensity maps

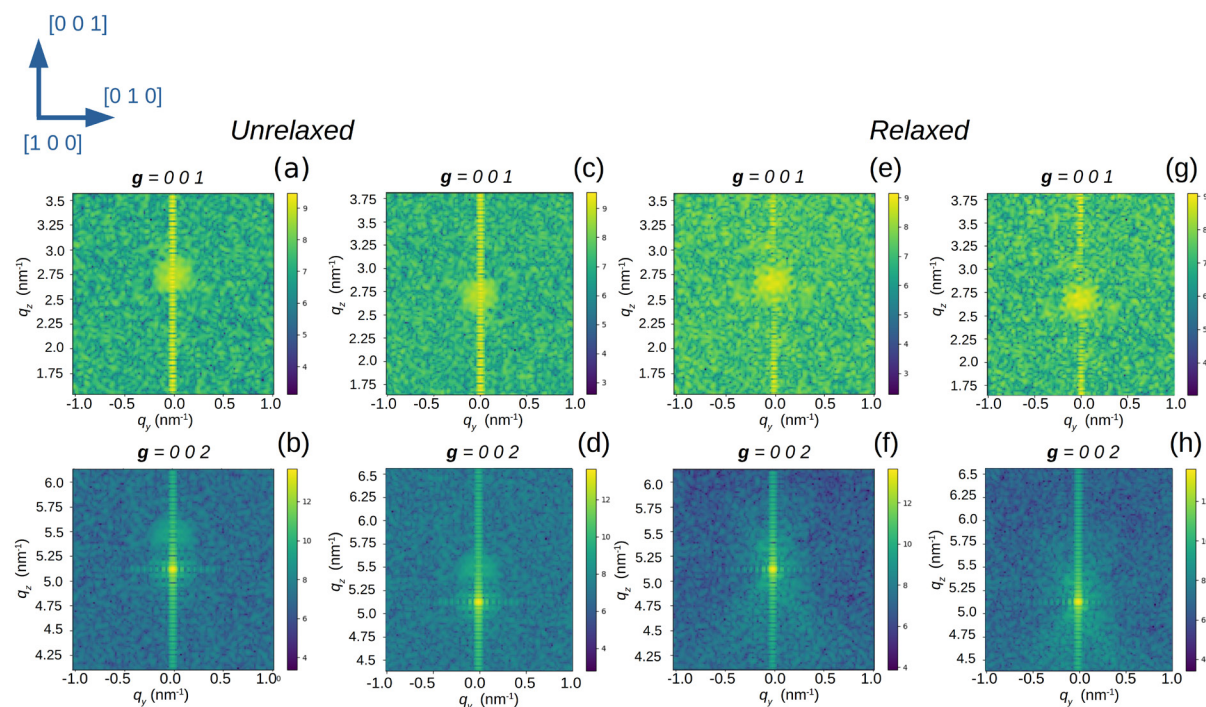


Figure S3 Slices of the reciprocal space intensity maps calculated for a single Ll_0 nanoprecipitate ($r = 2.5$ nm) coherently embedded in the disordered Al matrix. The calculations are performed before and after relaxation using different reference lattices. (a)-(b) Unrelaxed configuration and FCC reference lattice for a superstructure ($\mathbf{g} = 0\ 0\ 1$) and fundamental ($\mathbf{g} = 0\ 0\ 2$) reflection, respectively. (c)-(d) Unrelaxed configuration and FCT reference lattice for ($\mathbf{g} = 0\ 0\ 1$) and ($\mathbf{g} = 0\ 0\ 2$) respectively. (e)-(f) Relaxed configuration and FCC reference lattice for ($\mathbf{g} = 0\ 0\ 1$) and ($\mathbf{g} = 0\ 0\ 2$) respectively. (g)-(h) Relaxed configuration and FCT reference lattice for ($\mathbf{g} = 0\ 0\ 1$) and ($\mathbf{g} = 0\ 0\ 2$) respectively. The computation is performed over a RSV of $0.171 \times 0.171 \times 0.171\ \text{nm}^{-3}$ ($0.168 \times 0.168 \times 0.182\ \text{nm}^{-3}$) for the FCC (FCT) reference lattice respectively.

Figure S3 illustrates the choice of the reference lattice on the computed reciprocal space intensity map. The calculations are performed on a $22 \times 22 \times 22\ \text{nm}^3$ simulation cell containing a single coherent Ll_0 nanoprecipitate inserted in the centre of a disordered Al FCC matrix and the results are presented before and after relaxation in **Figure S3a-d** and **Figure S3e-h** respectively. The top row shows the scattered intensity around a superstructure reflection, $\mathbf{g} = 0\ 0\ 1$, while the bottom row shows the scattered intensity around a fundamental reflection, $\mathbf{g} = 0\ 0\ 2$. In good agreement with our previous observations, only the ordered phase scatters around $\mathbf{g} = 0\ 0\ 1$: a weak spherical intensity distribution consistent with the spherical shape of the nanoprecipitate can be observed. Around $\mathbf{g} = 0\ 0\ 2$, both ordered and disordered phases are scattering, the scattered intensity from the latter being much more intense because of the much larger volume fraction of the Al phase. Given the larger c -axis of the Al phase, the latter scatters at a lower q (for $\mathbf{g} = 0\ 0\ 2$, $q_z = 0.547\ \text{\AA}^{-1}$ and $q_z = 0.513\ \text{\AA}^{-1}$ for the ordered and disordered phases respectively). The calculations performed before relaxation illustrate well the

importance of the choice of the reference lattice. When using the reference FCC lattice ($a = 3.901 \text{ \AA}$), the computed RSV is centred around the intense peak scattered by the Al FCC matrix (**Figure S3b**). When using the FCT lattice as a reference on the other hand, the RSV is centred around the more diffuse spherical intensity distribution scattered by the nanoprecipitate (**Figures S3c,d**). Similar observations can be drawn after relaxation: independently of the choice of the reference lattice, the centre of mass of the Ll_0 nanoprecipitate peak moves towards lower q (for $\mathbf{g} = 0\ 0\ 1$, $q_z = 0.274 \text{ \AA}^{-1}$ and $q_z = 0.265 \text{ \AA}^{-1}$ before and after relaxation respectively) corresponding to an increase of the $\frac{c}{a}$ ratio from 0.92 to 0.96. The increasing of the diffuse scattering in the vicinity of the Ll_0 peak is induced by the inhomogeneous strain that builds up during relaxation (**Figures S3e-g**). Around $\mathbf{g} = 0\ 0\ 2$, the centre of mass of the disordered and ordered peaks being much closer after relaxation, the latter becomes difficult to distinguish because of the low volume fraction of the ordered phase and of the increased diffuse scattering.

S4. Evolution of the integrated intensities as a function of the order parameter**Table S3** Evolution of ($I_{int_001} / I_{int_002}$) for unrelaxed and relaxed atomistic configurations and (I_{th_001} / I_{th_002}) as a function of the order parameter S for a varying composition.

x_{Au}	x_{Cu}	S	Unrelax (25x25x33)	Relax (25x25x33)	Unrelax (75x75x100)	Relax (75x75x100)	$I_{th_001}/I_{th_002} (%)$
			$I_{int_001}/I_{int_002} (%)$	$I_{int_001}/I_{int_002} (%)$	$I_{int_001}/I_{int_002} (%)$	$I_{int_001}/I_{int_002} (%)$	
0.5	0.5	1	33.81	33.32	33.93	32.54	34.04
0.45	0.55	0.9	30.96	30.94	31.27	29.86	31.10
0.4	0.6	0.8	27.90	27.86	28.41	27.09	27.92
0.35	0.65	0.7	24.65	24.65	25.38	24.14	24.51
0.3	0.7	0.6	21.07	20.43	22.05	20.74	20.85
0.25	0.75	0.5	17.20	16.61	18.43	17.22	16.97
0.2	0.8	0.4	13.17	14.80	14.64	13.60	12.90
0.15	0.85	0.3	9.03	11.11	10.58	9.75	8.75
0.1	0.9	0.2	5.01	6.50	6.55	5.96	4.79
0.049	0.951	0.1	1.76	2.46	2.89	2.57	1.52
0.025	0.975	0.05	0.67	0.69	-	-	0.43
0.005	0.995	0.01	0.22	0.06	0.42	0.23	0.02
0.001	0.999	0.002	0.20	0.02	-	-	0.00
0.0001	0.9999	0.0002	0.19	0.01	-	-	0.00

Table S4 Evolution of ($I_{int_001} / I_{int_002}$) and (I_{th_001} / I_{th_002}) for unrelaxed and relaxed atomistic configurations as a function of the order parameter S for a fixed composition.

x_{Au}	x_{Cu}	S	Unrelax (25x25x33)	Relax (25x25x33)	Unrelax (75x75x100)	Relax (75x75x100)	$I_{th_001}/I_{th_002} (%)$
			$I_{int_001}/I_{int_002} (%)$	$I_{int_001}/I_{int_002} (%)$	$I_{int_001}/I_{int_002} (%)$	$I_{int_001}/I_{int_002} (%)$	
0.5	0.5	0.5	9.13	8.83	10.25	9.43	8.57
0.5	0.5	0.33	4.46	3.90	5.80	5.04	3.81
0.5	0.5	0.2	2.14	1.42	3.60	2.84	1.36
0.5	0.5	0.1	1.18	0.41	2.69	1.94	0.34
0.5	0.5	0	0.88	0.09	2.42	1.69	0.00

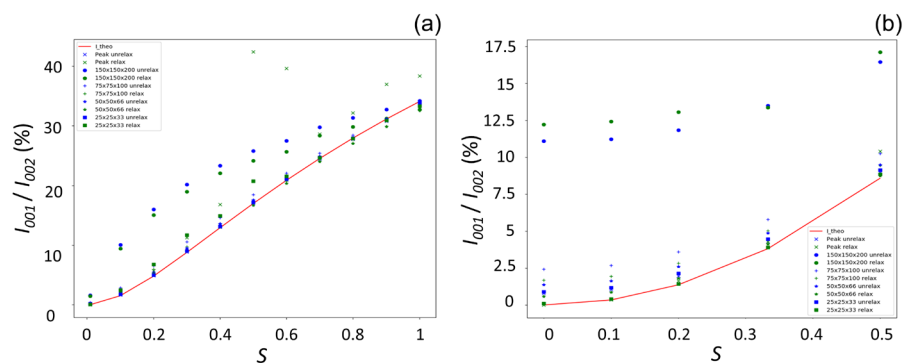


Figure S4 Evolution of $(I_{int_001} / I_{int_002})$ and $(I_{th_001} / I_{th_002})$ for the unrelaxed and relaxed configurations as a function of the order parameter S for a varying composition (a) and a fixed composition (b). In both cases, the calculations are carried out on the large RSV (150x150x200 RSPs) and the integrations are performed over RSVs ranging from 25x25x30 RSPs to 150x150x200 RSPs.

S5. Evolution of the integrated amplitudes and electron densities as a function of the order parameter

Table S5 Evolution of $(\rho_{int_001} / \rho_{int_002})$ and $(A_{int_001} / A_{int_002})$ for unrelaxed and relaxed atomistic configurations and $(A_{th_001} / A_{th_002})$ as a function of the order parameter S for a varying composition. The results are given for the small RSV / large voxel size (1.09 nm). The integration is performed over 25x25x33 RSPs while the threshold for the integrated electron density is set at 25% of the maximum value

S	Unrelax	Relax	Unrelax	Relax	A_{th_001} / A_{th_002}
	$\rho_{int_001} / \rho_{int_002} (25\%)$	$\rho_{int_001} / \rho_{int_002} (25\%)$	$A_{int_001} / A_{int_002}$	$A_{int_001} / A_{int_002}$	
1	58.08	56.95	58.15	57.73	58.35
0.9	55.69	54.66	55.64	55.63	55.77
0.8	52.87	51.92	52.82	52.79	52.84
0.7	49.71	48.78	49.65	49.65	49.51
0.6	46.01	44.55	45.91	45.20	45.67
0.5	41.60	40.34	41.47	40.76	41.19
0.4	36.56	35.22	36.30	38.47	35.91
0.3	30.37	28.87	30.05	33.33	29.59
0.2	22.82	21.49	22.39	25.49	21.88
0.1	14.01	12.83	13.28	15.69	12.32
0.05	9.11	7.64	8.16	8.33	6.55
0.01	5.70	2.91	4.73	2.51	1.38
0.002	5.25	1.81	4.42	1.33	0.28
0.0002	5.17	1.66	4.38	1.16	0.03

Table S6 Evolution of $(\rho_{int_001} / \rho_{int_002})$ and $(A_{int_001} / A_{int_002})$ for unrelaxed and relaxed atomistic configurations and $(A_{th_001} / A_{th_002})$ as a function of the order parameter S for a fixed composition. The results are given for the small RSV / large voxel size (1.09 nm). The integration is performed over 25x25x33 RSPs while the threshold for the integrated electron density is set at 25% of the maximum value

S	Unrelax	Relax	Unrelax	Relax	A_{th_001} / A_{th_002}
	$\rho_{int_001} / \rho_{int_002} (25\%)$	$\rho_{int_001} / \rho_{int_002} (25\%)$	$A_{int_001} / A_{int_002}$	$A_{int_001} / A_{int_002}$	
0.5	30.91	29.47	30.22	29.72	29.28
0.33	22.33	20.16	21.12	19.74	19.52
0.2	16.64	13.10	14.61	11.92	11.67
0.1	13.66	9.05	10.85	6.41	5.83
0	12.72	7.52	9.40	2.98	0.00

Table S7 Evolution of ($\rho_{int_001} / \rho_{int_002}$) and ($A_{int_001} / A_{int_002}$) for unrelaxed and relaxed atomistic configurations and (A_{th_001} / A_{th_002}) as a function of the order parameter S for a varying composition. The results are given for the small RSV / small voxel size (0.357 nm). The integration is performed over 75x75x100 RSPs while the threshold for the integrated electron density is set at 12.5% of the maximum value

<i>S</i>	Unrelax	Relax	Unrelax	Relax	A_{th_001} / A_{th_002}
	$\rho_{int_001} / \rho_{int_002}$ (12.5%)	$\rho_{int_001} / \rho_{int_002}$ (12.5%)	$A_{int_001} / A_{int_002}$	$A_{int_001} / A_{int_002}$	
1	58.64	57.01	58.25	57.05	58.35
0.9	56.10	54.45	55.92	54.65	55.77
0.8	53.24	51.57	53.31	52.05	52.84
0.7	49.83	48.49	50.38	49.13	49.51
0.6	46.42	45.22	46.96	45.54	45.67
0.5	42.60	41.09	42.93	41.50	41.19
0.4	38.14	36.95	38.26	36.87	35.91
0.3	32.15	31.04	32.52	31.22	29.59
0.2	25.61	23.53	28.79	24.41	21.88
0.1	16.03	15.39	17.01	16.04	12.32
0.01	2.30	2.37	6.49	4.83	1.38

Table S8 Evolution of ($\rho_{int_001} / \rho_{int_002}$) and ($A_{int_001} / A_{int_002}$) for unrelaxed and relaxed atomistic configurations and (A_{th_001} / A_{th_002}) as a function of the order parameter S for a fixed composition. The results are given for the large RSV / small voxel size (0.357 nm). The integration is performed over 75x75x100 RSPs while the threshold for the integrated electron density is set at 25% of the maximum value

<i>S</i>	Unrelax	Relax	Unrelax	Relax	A_{th_001} / A_{th_002}
	$\rho_{int_001} / \rho_{int_002}$ (25%)	$\rho_{int_001} / \rho_{int_002}$ (25%)	$A_{int_001} / A_{int_002}$	$A_{int_001} / A_{int_002}$	
0.5	29.17	28.59	32.01	30.70	29.28
0.33	23.02	22.96	24.08	22.44	19.52
0.2	21.26	20.59	18.98	16.86	11.67
0.1	19.77	20.09	16.39	13.93	5.83
0	18.78	19.29	15.55	12.99	0.00

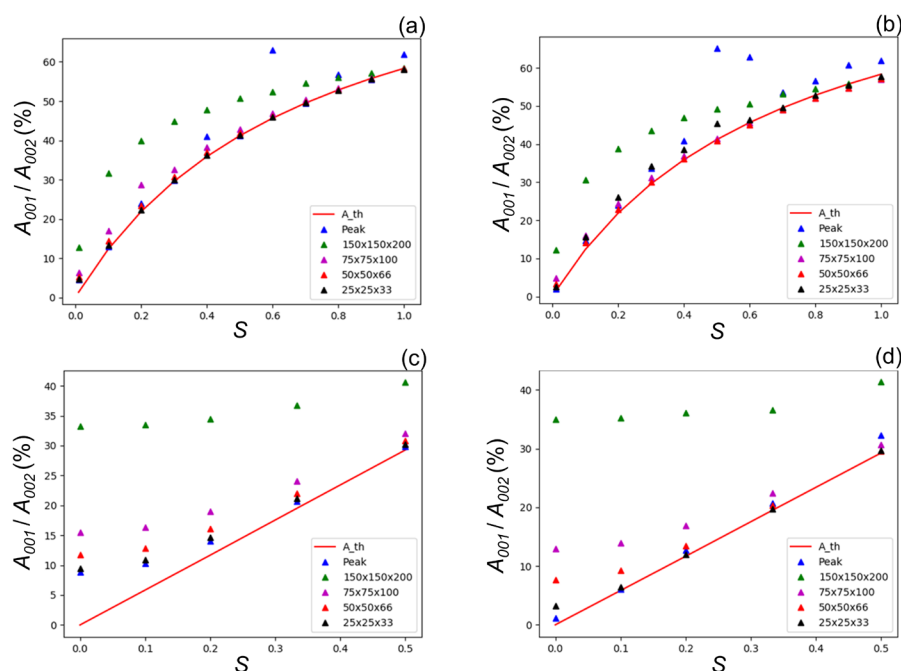


Figure S5 Evolution of $(A_{int_001} / A_{int_002})$ and $(A_{th_001} / A_{th_002})$ as a function of the order parameter S for a varying atomic composition before (a) and after (b) relaxation. Same ratios as a function of S for a fixed composition before (c) and after (d) relaxation. In both cases, the calculations are carried out on the large RSV (150x150x200 RSPs) and the integrations are performed over RSVs ranging from 25x25x30 RSPs to 150x150x200 RSPs.

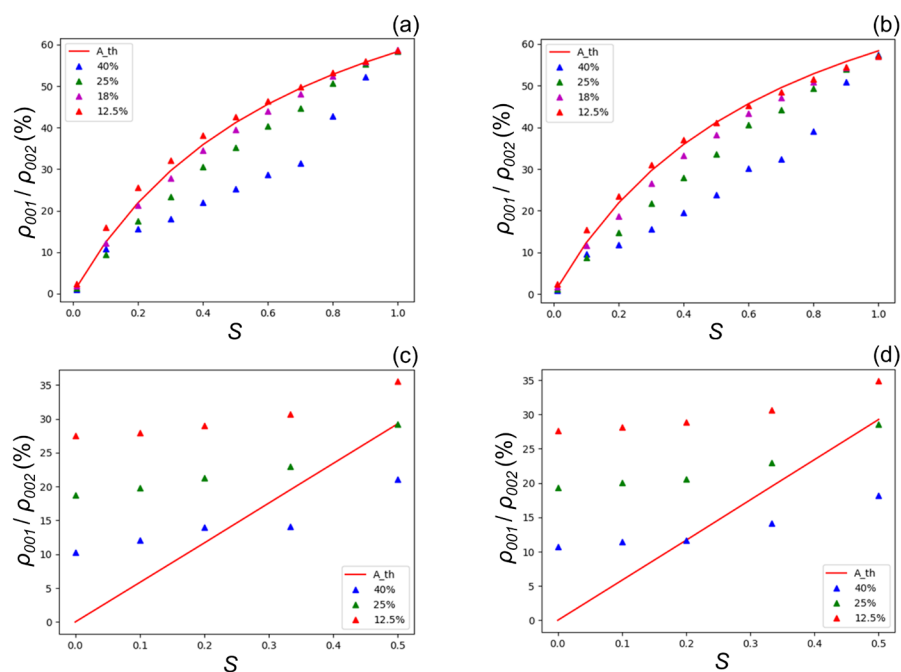


Figure S6 Evolution of $(\rho_{int_001} / \rho_{int_002})$ and $(A_{th_001} / A_{th_002})$ as a function of the order parameter S for a varying atomic composition before (a) and after (b) relaxation. Same ratios as a function of S for a fixed composition before (c) and after (d) relaxation. In both cases, the calculations are carried out on the large RSV (150x150x200 RSPs) and the integrations are performed over RSVs ranging from 25x25x30 RSPs to 150x150x200 RSPs.

S6. Evolution of the calculated order parameter as a function of the order parameter

Table S9 Evolution of the order parameter calculated from the ratio of the integrated intensities as compared to the theoretical order parameter for the relaxed and unrelaxed configurations with a varying composition. In both cases, the calculations are carried out on the small RSV (50x50x66 RSPs) and the integrations are performed over 25x25x30 and 50x50x66 RSPs.

S_{theory}	S relaxed 50x50x66	S unrelaxed 50x50x66	S relaxed 25x25x33	S unrelaxed 25x25x33
1	0.979	0.997	0.989	0.997
0.9	0.882	0.900	0.898	0.898
0.8	0.787	0.802	0.799	0.800
0.7	0.692	0.705	0.702	0.702
0.6	0.593	0.607	0.594	0.603
0.5	0.496	0.509	0.495	0.503
0.4	0.402	0.411	0.428	0.404
0.3	0.305	0.312	0.338	0.305
0.2	0.210	0.214	0.233	0.205
0.1	0.115	0.117	0.127	0.108
0.05	0.065	0.071	0.064	0.062
0.01	0.024	0.039	0.018	0.034
0.002	0.014	0.034	0.010	0.032
0.0002	0.013	0.033	0.008	0.031

Table S10 Evolution of the order parameter calculated from the ratio of the integrated intensities as compared to the theoretical order parameter for the relaxed and unrelaxed configurations with a fixed composition. In both cases, the calculations are carried out on the small RSV (50x50x66 RSPs) and the integrations are performed over 25x25x30 and 50x50x66 RSPs.

S_{theory}	S relaxed 50x50x66	S unrelaxed 50x50x66	S relaxed 25x25x33	S unrelaxed 25x25x33
0.5	0.506	0.526	0.508	0.516
0.3334	0.347	0.377	0.337	0.361
0.2	0.231	0.275	0.204	0.250
0.1	0.159	0.219	0.110	0.186
0	0.131	0.200	0.051	0.161

Table S11 Evolution of the order parameter calculated from the ratio of the integrated and peak intensities, as compared to the theoretical order parameter for relaxed and unrelaxed configurations with a varying composition. In both cases, the calculations are carried out on the large RSV (150x150x200 RSPs) and the integration is performed over 75x75x100 RSPs.

S_{theory}	S relaxed 75x75x100	S unrelaxed 75x75x100	S relaxed peak	S unrelaxed peak
1	0.978	0.998	1.061	0.994
0.9	0.882	0.902	0.981	0.896
0.8	0.788	0.807	0.859	0.797
0.7	0.695	0.712	0.756	0.699
0.6	0.598	0.617	0.827	0.601
0.5	0.504	0.521	0.790	0.501
0.4	0.411	0.426	0.457	0.402
0.3	0.317	0.330	0.341	0.302
0.2	0.223	0.234	0.219	0.202
0.1	0.131	0.138	0.119	0.105
0.01	0.035	0.047	0.015	0.033

Table S12 Evolution of the order parameter calculated from the ratio of the integrated and peak intensities, as compared to the theoretical order parameter for relaxed and unrelaxed configurations with a fixed composition. In both cases, the calculations are carried out on the large RSV (150x150x200 RSPs) and the integration is performed over 75x75x100 RSPs.

S_{theory}	S relaxed 75x75x100	S unrelaxed 75x75x100	S relaxed peak	S unrelaxed peak
0.5	0.524	0.547	0.551	0.511
0.3334	0.383	0.411	0.354	0.354
0.2	0.289	0.325	0.218	0.241
0.1	0.239	0.281	0.104	0.176
0	0.223	0.266	0.020	0.152

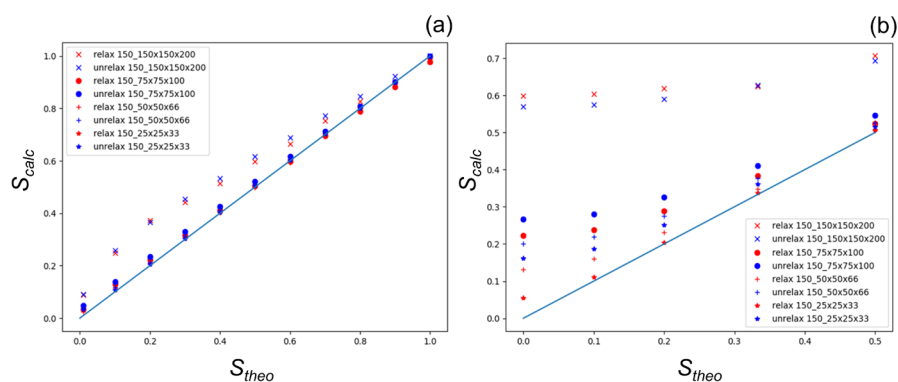


Figure S7 Evolution of the order parameter calculated from the ratio of the integrated intensities (S_{calc} , equation (9)) as a function of the theoretical order parameter (S_{theo} , equation (3)) for the varying (a) and fixed (b) compositions. In both cases, the calculations are carried out on the large RSV (150x150x200 RSPs) and the integrations are performed over RSVs ranging from 25x25x33 RSPs to 150x150x200 RSPs.

S7. Evolution of the Pearson correlation function r as a function of the order parameter**Table S13** Evolution of the Pearson correlation function between the ε_{001} retrieved from the superstructure ($\mathbf{g} = 0\ 0\ 1$) and the fundamental ($\mathbf{g} = 0\ 0\ 2$) reflections as a function of the order parameter S for the varying composition.

x_{Au}	x_{Cu}	S	Relax small RSV	Unrelax small RSV	Relax large RSV	Unrelax large RSV
0.5	0.5	1	0.994	0.968	0.998	0.997
0.45	0.55	0.9	0.958	0.974	0.958	0.935
0.4	0.6	0.8	0.963	0.998	0.792	0.893
0.35	0.65	0.7	0.918	0.966	0.804	0.827
0.3	0.7	0.6	0.997	0.997	0.780	0.887
0.25	0.75	0.5	0.995	0.995	0.742	0.744
0.2	0.8	0.4	0.988	0.992	0.544	0.443
0.15	0.85	0.3	0.982	0.986	0.512	0.499
0.1	0.9	0.2	0.961	0.970	0.380	0.287
0.049	0.951	0.1	0.919	0.887	0.220	0.243
0.025	0.975	0.05	0.837	0.923	-	-
0.005	0.995	0.01	0.703	0.926	0.155	0.099
0.001	0.999	0.002	0.570	0.949	-	-
0.0001	0.9999	0.0002	0.488	0.907	-	-

Table S14 Evolution of the Pearson correlation function between the ε_{001} retrieved from the superstructure ($\mathbf{g} = 0\ 0\ 1$) and the fundamental ($\mathbf{g} = 0\ 0\ 2$) reflections as a function of the order parameter S for the fixed composition.

x_{Au}	x_{Cu}	S	Relax small RSV	Unrelax small RSV	Relax large RSV	Unrelax large RSV
0.5	0.5	0.5	0.915	0.855	0.596	0.687
0.5	0.5	0.33	0.885	0.914	0.516	0.517
0.5	0.5	0.2	0.849	0.932	0.505	0.520
0.5	0.5	0.1	0.727	0.884	0.458	0.500
0.5	0.5	0	0.735	0.919	0.482	0.487

S8. Success rate of the phase retrieval as a function of the number of precipitates: Influence of the choice of the threshold for the shrink-wrap**Table S15** Influence of the choice of the threshold for the shrink-wrap on the success rate of the phase retrieval

	<i>N</i> <i>precipitates</i>	Crystal size (nm ³)	Oversampling	Radius precipitate (nm)	Voxel size (nm)	Success rate (%)	Threshold shrink wrap
Unrelaxed	2	22x22x22	32.4	2.5	0.436	0	0.42-0.44
Unrelaxed	2	22x22x22	32.4	2.5	0.436	99	0.27-0.37
Unrelaxed	8	22x22x22	18.7	1.5-2.8	0.492	64	0.33-0.37
Unrelaxed	8	22x22x22	18.7	1.5-2.8	0.492	88	0.365-0.40
Relaxed	8	22x22x22	18.7	1.5-2.8	0.492	52	0.33-0.37
Relaxed	8	22x22x22	18.7	1.5-2.8	0.492	92	0.365-0.40
Unrelaxed	48	66x66x66	8.4	1.5-2.8	1.15	36	0.42-0.44
Unrelaxed	48	66x66x66	8.4	1.5-2.8	1.15	82	0.36-0.40

S9. Intensity scattered by a varying number of coherent nanoprecipitates in the vicinity of a superstructure reflection

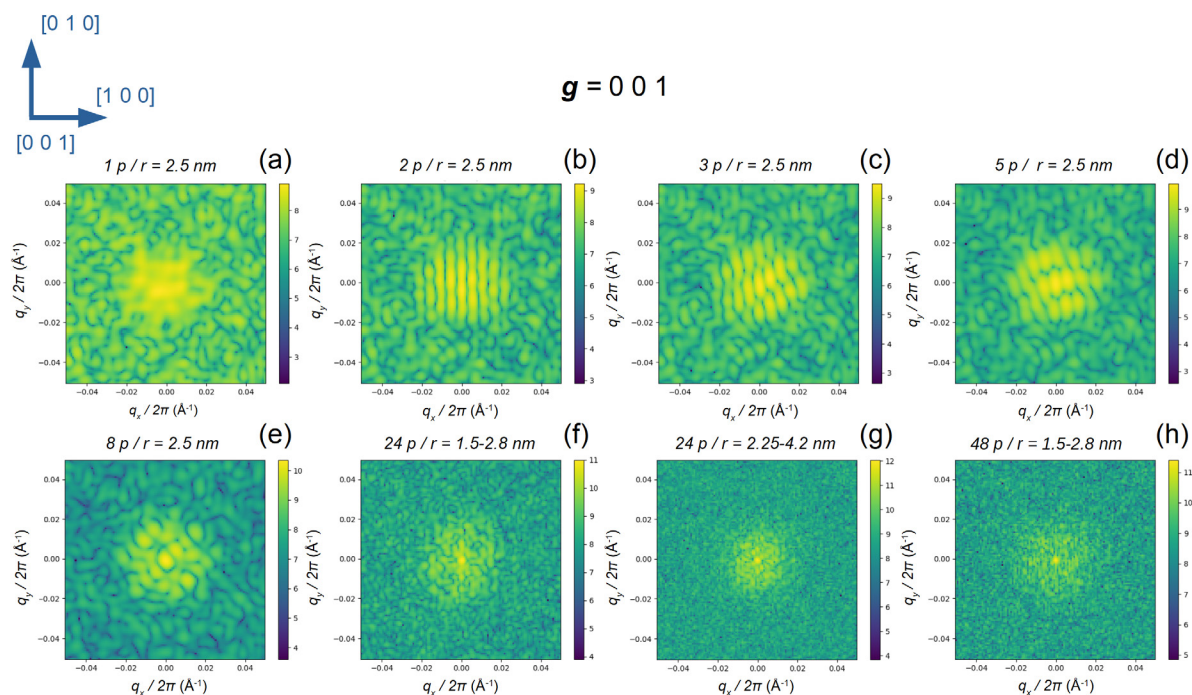


Figure S8 Slice of the intensity scattered by a varying number of coherent nanoprecipitates in the vicinity of the superstructure reflection, ($g = 0\ 0\ 1$). The number of nanoprecipitates and their radius are indicated above the figures. All the calculations are performed on relaxed configurations. The size of the simulation cell varies between $22 \times 22 \times 22$ nm³ (a-e), $44 \times 44 \times 44$ nm³ (f) and $66 \times 66 \times 66$ nm³. The RSV is kept constant in all figures and is equal to $0.084 \times 0.084 \times 0.091$ nm⁻³.

S10. Influence of the dynamical range on the retrieved displacement field

A very high dynamical range (ratio between the maximum of intensity and the minimum of intensity) is used in the simulations presented in the manuscript, ranging typically between 12 and 14 decades of intensities. Such high dynamical range is of course not accessible experimentally. In modern synchrotrons, the intensity diffracted by a nanostructure spans typically 3 to 6 decades of intensities. To assess the influence of the dynamical range on the retrieved real space image, we varied the dynamical range between 3 and 6 decades of intensities and compared it with the real space image obtained with the full dynamical range (12 to 14 decades of intensities). The simulated configuration is a FCT LI_0 simulation cell ($11 \times 11 \times 31 \text{ nm}^3$, $S = 0.5$).

Figure S9-S12 show the calculated scattered intensities and the corresponding retrieved real space displacement for $\mathbf{g} = 0\ 0\ 1$ and $\mathbf{g} = 0\ 0\ 2$. The q ranges considered for the calculation are the same as the ones used in section 3.2: $0.827 \times 0.827 \times 1.19 \text{ nm}^{-3}$ and $2.51 \times 2.51 \times 3.64 \text{ nm}^{-3}$ for the small and large q ranges respectively. As a reminder, these q ranges translate to an average real space voxel size of 1.09 nm and 0.357 nm, respectively.

For the small q -range / RSV, the retrieved displacement is not affected by the dynamical range when the latter is higher or equal to 4 decades of intensity (**Figures S9g-j** & **Figures S10g-j**). For 3 decades of intensity, the real space spatial resolution starts to deteriorate because of the loss of the high frequency information (high q range, **Figures S9a,f** & **Figures S10a,f**). Note that these observations are valid for both superstructure (**Figure S9**) and fundamental reflections (**Figure S10**).

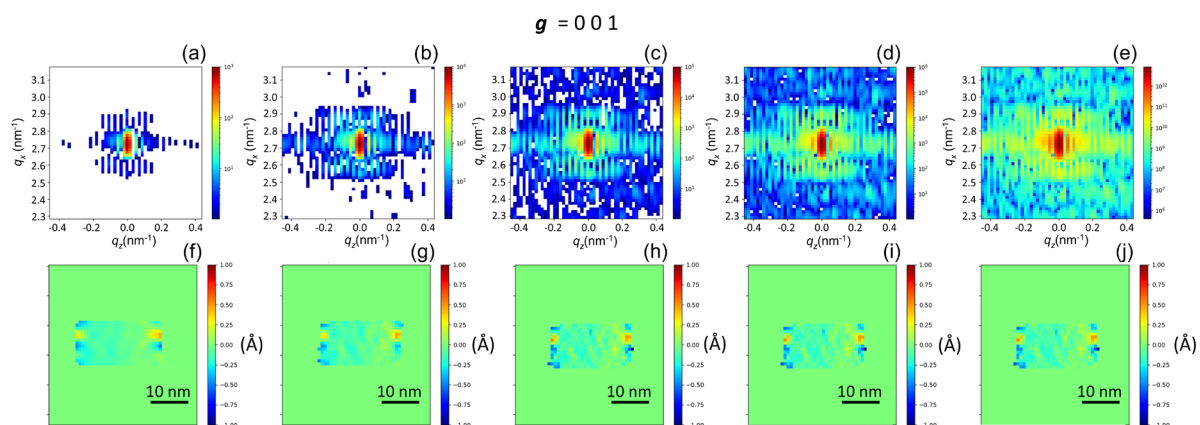


Figure S9 Influence of the dynamical range on the retrieved displacement for a small q range ($0.827 \times 0.827 \times 1.19 \text{ nm}^{-3}$) and $\mathbf{g} = 0\ 0\ 1$. (a) $I_{\max} = 10^3$, (b) $I_{\max} = 10^4$, (c) $I_{\max} = 10^5$, (d) $I_{\max} = 10^6$, (e) $I_{\max} = 8.10^{12}$. (f-j) Corresponding retrieved displacement (average real space voxel size = 1.09 nm).

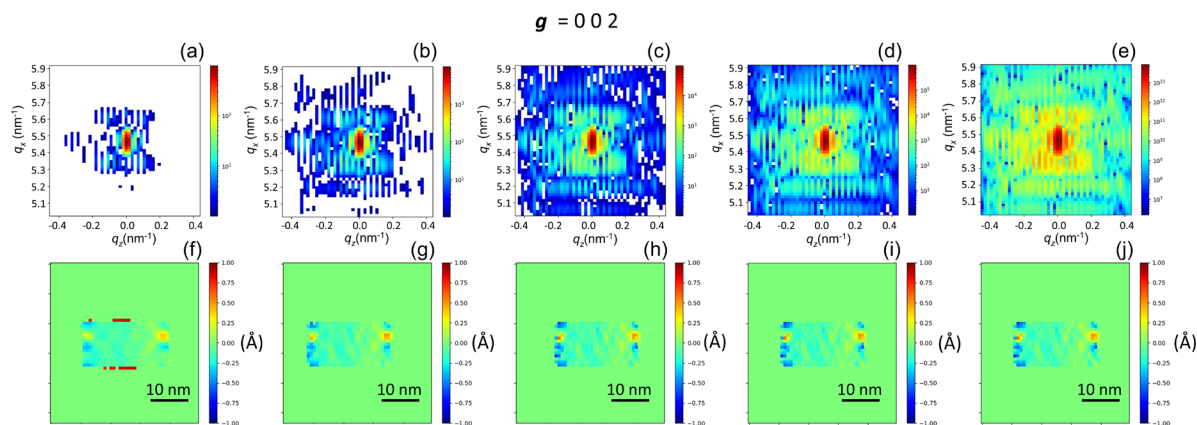


Figure S10 Influence of the dynamical range on the retrieved displacement for a small q range ($0.827 \times 0.827 \times 1.19 \text{ nm}^{-3}$) and $g = 0.02$. (a) $I_{\max} = 10^3$, (b) $I_{\max} = 10^4$, (c) $I_{\max} = 10^5$, (d) $I_{\max} = 10^6$, (e) $I_{\max} = 8.10^{13}$. (f-j) Corresponding retrieved displacement (average real space voxel size = 1.09 nm).

For the large q range / RSV, the spatial resolution starts to be affected for 5 decades of intensity. The calculations performed for 3 and 4 decades of intensity show a notable deterioration of the spatial resolution in the real space (**Figures S11f,g** & **Figures S12f,g**)

This outcome was to be expected since regions further away from the Bragg peak are included in the calculation for the large q range, hence the higher sensitivity to the dynamical range. Also, interestingly, for $g = 0.01$, decreasing the dynamical range is equivalent as applying a low pass filter: below 4 decades of intensity there are very few pixels where the phase is not retrieved accurately.

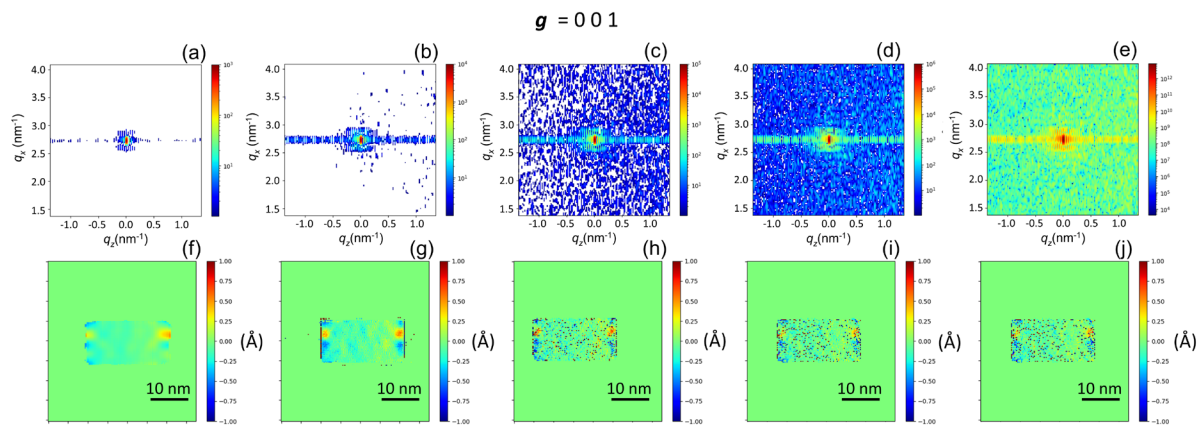


Figure S11 Influence of the dynamical range on the retrieved displacement for a large q range ($2.51 \times 2.51 \times 3.64 \text{ nm}^{-3}$) and $g = 0.01$. (a) $I_{\max} = 10^3$, (b) $I_{\max} = 10^4$, (c) $I_{\max} = 10^5$, (d) $I_{\max} = 10^6$, (e) $I_{\max} = 8.10^{12}$. (f-j) Corresponding retrieved displacement (average real space voxel size = 0.357 nm).

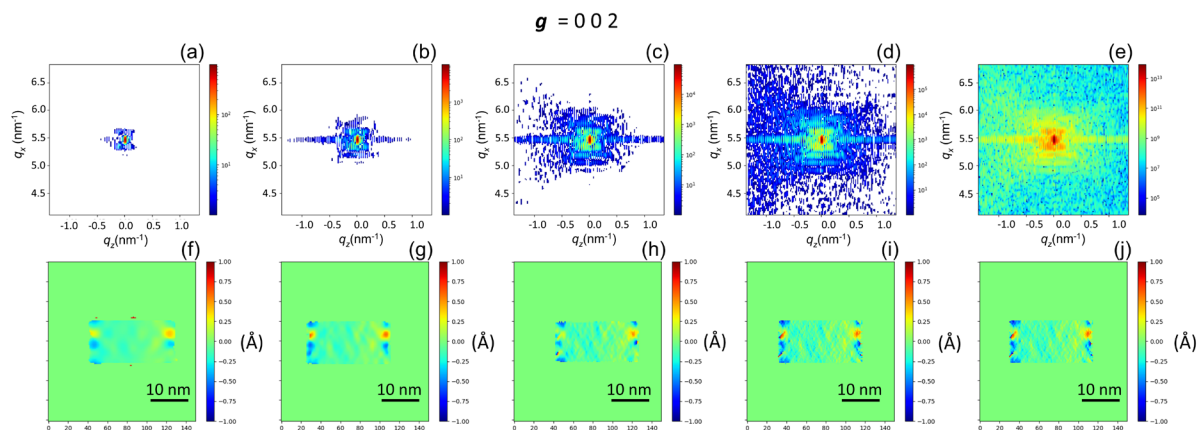


Figure S12 Influence of the dynamical range on the retrieved displacement for a large q range ($2.51 \times 2.51 \times 3.64 \text{ nm}^{-3}$) and $g = 0\ 0\ 2$. (a) $I_{\max} = 10^3$, (b) $I_{\max} = 10^4$, (c) $I_{\max} = 10^5$, (d) $I_{\max} = 10^6$, (e) $I_{\max} = 8.10^{13}$. (f-j) Corresponding retrieved displacement (average real space voxel size = 0.357 nm).

S11. Accuracy of the strain field predicted by the molecular statics simulations

As indicated in section 3.1, the ε_{001} strain component obtained from the molecular statics (MS) simulations was compared with experimental values obtained from synchrotron powder X-ray diffraction measurements carried out by (Garcia-Gonzalez *et al.*, 2020). By following the position and Full Width Half Maximum (FWHM) of several superstructure peaks during heating of the sample, the authors were able to evidence that the evolution of the several strain components, including ε_{001} was not monotonous. An initial increase of the tensile strain of the ordered LI_0 phase up to 3.5% was followed by a decrease above $T = 300^\circ\text{C}$. As shown in **Figure S13**, this trend was captured at least qualitatively by the MS simulations performed for precipitates sizes ranging between 0.75 and 5.5 nm. An initial increase of the tensile strain, with a maximum reached for a radius of $r = 1.7$ nm ($\overline{\varepsilon_{001}} = 4.1\%$) is followed by a strain relaxation for $r > 1.7$ nm (**Figure S13a**). The maximum tensile strain obtained from the MS simulations is consistent with the experimental data ($\overline{\varepsilon_{001}} = 3.5\%$, **Figure S13b**). Note that the evolution of the other strain components, ε_{112} , (**Figure S13c**) and ε_{201} , (**Figure S13c**) is also fairly well predicted by the MS simulations.

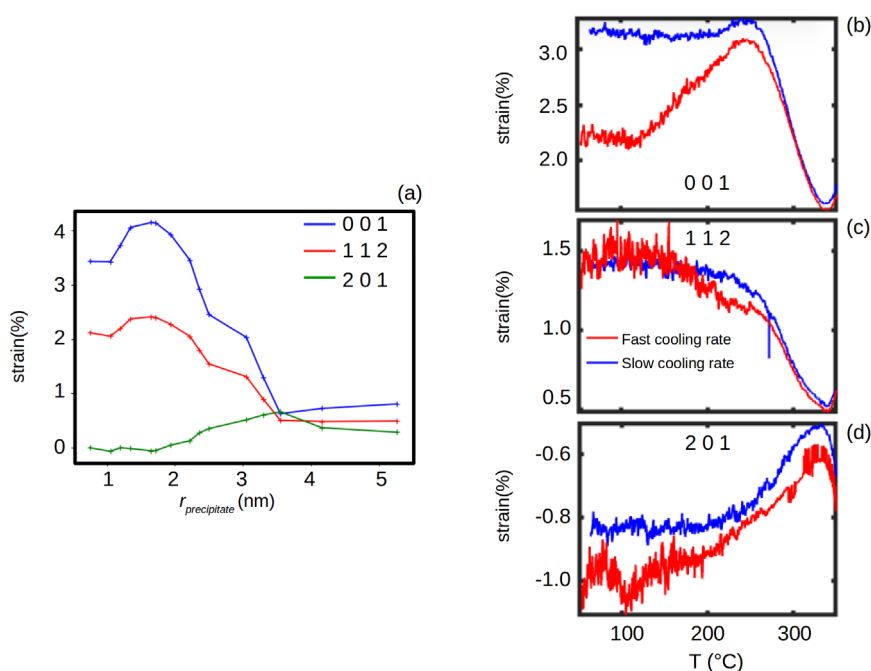


Figure S13 (a) Evolution of several strain components as a function of the precipitate radius obtained from MS simulations (b) –(d) Lattice strain evolution as a function of temperature for several superstructure peaks obtained from *in situ* X-ray powder diffraction experiments (Fast cooling rate: $-800^\circ\text{C}/\text{min}$, slow cooling rate: $-100^\circ\text{C}/\text{min}$).